Available online at www.sciencedirect.com

jmr&t Journal of Materials Research and Technology

journal homepage: www.elsevier.com/locate/jmrt

Original Article

Microstructure and mechanical properties of Cu–Fe-ZTA cermets prepared by vacuum hot pressing sintering

Qi Gao [a,b], Daming Sun [c,**], Xiaosong Jiang [a,b,*], Hongliang Sun [a,b], Yali Zhang [d], Yongjian Fang [d], Rui Shu [e]

[a] Key Laboratory of Advanced Technologies of Materials, Ministry of Education, Chengdu 610031, China
[b] School of Materials Science and Engineering, Southwest Jiaotong University, Chengdu Sichuan 610031, China
[c] Department of Chemistry and Bioscience, Aalborg University, Aalborg, 9220, Denmark
[d] School of Mechanical Engineering, Sungkyunkwan University, 2066 Seobu-ro, Jangan-gu, Suwon-si, Gyeonggi-do, 16419, Republic of Korea
[e] Forschungszentrum Jülich GmbHInstitut für Energie-und Klimaforschung Plasmaphysik (IEK-4), 52425 Jülich, Germany

ARTICLE INFO

Article history:
Received 22 May 2022
Accepted 26 July 2022
Available online 13 August 2022

Keywords:
ZTA
Cermet
Vacuum hot pressing sintering
Powder metallurgy
Interface bonding
Wear performance

ABSTRACT

Cermets with Cu and Fe as matrix and zirconia toughened alumina (ZTA) as reinforcement phase were prepared by vacuum hot pressing sintering. Electroless Ni plating was carried out on ZTA particles to improve the interfacial bonding ability between ZTA and metal matrix. Cu-xFe-ZTA cermets (x = 20, 50, 80) were prepared by using different proportions of Cu powders and Fe powders as the binder in order to investigate the influence of binder types on the grinding performance of cermets. The phase composition, microstructure, mechanical properties and grinding properties of Cu–Fe-ZTA cermets were systematically studied. It revealed that the difference of cermet grinding performance lay in the bonding force between metal matrix and abrasive. The coating ability of abrasive is stronger with the increase of Cu content in the matrix. Because the matrix is soft and easy to grind, the cermet grinding wheel material has strong self-sharpening, and Cu–20Fe-ZTA grinding effect is the best. The friction coefficient of Cu–20Fe-ZTA cermets was 0.405, the grinding surface roughness was 7.972 μm, and the residual stress σ_x and σ_y were 180.5 and 89.6 MPa, respectively. As the Fe content decreased, the grinding mechanism changed from ploughing and cutting to friction.

* Corresponding author.
** Corresponding author.
E-mail addresses: damings@bio.aau.dk (D. Sun), xsjiang@swjtu.edu.cn (X. Jiang).

https://doi.org/10.1016/j.jmrt.2022.07.151

1. Introduction

Wear is one of the most important failure modes of material loss in construction, railway and shipbuilding applications [1,2]. For example, increasing capacity and speed lead to defects such as pitting corrosion, ripples and cracks in rails in a short period of time, which can extend into the interior of rails and pose a great threat to safe operation [3,4]. Using rail grinding to maintain the railway can eliminate these adverse effects. Surface defects such as corrugations and cracks can be removed through grinding to reduce wheel-rail contact stress, alleviate the plastic flow and contact fatigue of rail surface materials [5,6], avoid premature replacement of rail and reduce costs. In order to further improve grinding efficiency and obtain good surface integrity, the scientific research of rail grinding wheel/grindstone material itself is also of great significance.

Cermets are widely used as grinding wheel materials because of their high bonding strength, good formability and strong wear resistance [1]. At present, most researches on metal-based ceramic grinding wheel materials focus on single metal matrix, such as Cu, Fe and so on. Cu has the advantages of low cost, high thermal conductivity and good toughness [7,8], while Fe has the characteristics of high hardness, high wear resistance and good fatigue resistance [9,10]. According to the phase diagram, Fe and Cu are mutually soluble, and Cu–Fe alloy can combine their excellent properties well [11]. In addition, Cu–Fe is an amplitude-modulated system, which is almost immiscible at equilibrium at room temperature and has a positive enthalpy of mixing [12]. Using Cu–Fe as matrix, the strengthening mechanism is grain boundary strengthening and dislocation strengthening [13]. Cu–Fe matrix can combine the excellent properties of the two to meet the requirements of tool manufacturing and high wear resistance tool field [14]. Cermet materials reinforced with ZTA have excellent toughness of metal materials, excellent wear resistance and chemical stability of ceramic materials [15]. The reason is that ZrO_2 contained in ZTA will change from tetragonal system t-ZrO_2 to monoclical system m-ZrO_2 when subjected to stress, which consumes the energy of crack propagation and thus improves the toughness of cermets [16,17]. Moreover, the toughness of ZTA is several times that of pure Al_2O_3 ceramics [18], and the thermal expansion coefficient is closer to Fe matrix [17], which can avoid the generation of stress. In addition, in order to improve the interface bonding ability and improve the wetting effect, metal coating is used to modify ZTA particles to solve the problem that Al_2O_3 and ZrO_2 are polar materials with weak interface bonding ability of metal materials [19,20]. Ru et al. [19] found that Ni-coated ZTA particles reduced the wetting angle with Fe matrix. The Ni atoms diffuse into the Fe matrix, and the liquid metal penetrates into the depressions and pores on the surface of ZTA, forming a dense structural layer, thus improving the interface bonding strength. Sun et al. [8] found that electroless Ni plating can significantly improve the binding ability of ZTA particles to Cu matrix, resulting in a higher material removal rate of Cu-ZTA cermets. In addition to improving the interface wettability, suitable sintering process can also improve the interfacial bonding ability of ZTA, Cu and Fe. Shabani et al. [21] conducted dry sliding wear tests on the composites prepared and found that compared with the traditional sintering process, the compressive stress applied in the sintering process increases the density of the sample, improves the hardness and reduces the wear amount. Vacuum hot pressing (VHP) is a new process for manufacturing cermets [15]. It achieves the combination of reaction synthesis and densification through heating and pressurization, and has the advantages of high relative density and clean product interface, which can effectively solve the problem of low cermets forming rate [1]. Ji et al. [22] prepared Ni bonded Ti(C, N)-based ceramics using VHPs. Due to diffusion, Ti(C, N) particles dissolve in the Ni matrix to form edge phase, which improves the wettability between the finishing agent and the ceramics.

Therefore, in this paper, Cu–Fe-ZTA cermet material was creatively prepared by VHP sintering using mixed metal powder of Cu and Fe as binder. Electroless Ni plating was used to improve the bonding ability of ZTA and Cu–Fe matrix, balance thermal expansion coefficient difference between materials, and strengthen solid solution [8]. The effects of metal binder with different proportions on the properties of Cu–Fe-ZTA cermets were studied, and the rail grinding tests of Cu–Fe-ZTA cermets were carried out on a self-designed grinding device. Furthermore, the grinding mechanism and rail surface integrity of Cu–Fe-ZTA cermets were discussed.

2. Materials and methods

2.1. Raw materials and preparation

Three kinds of Cu-xFe-ZTA cermets with different metal binder contents were designed in this experiment (x = 20, 50, 80). ZTA particles with a diameter of 1.18 mm (F16) were used as the abrasive, and Cu and Fe powder mixed powder metal bond was used as the matrix of cermet grinding wheel (reinforced by FeS_2, Na_3AlF_6, TiH_2, $CaCO_3$, La, Cr, graphite, WC). The Cu, Fe and compounds used in this study were provided by Shanghai Naiou Nano Technology Co., Ltd. The effect of cement ratio on mechanical properties and grinding properties of cermets was studied. The specific parameters are shown in Table 1.

The preparation process of cermet grinding wheel materials in this paper mainly consists of several parts. First, raw

Table 1 – Composition of Cu–Fe-ZTA cermet (wt.%).

Number	Binder (Cu:Fe)	ZTA	FeS_2	Na_3AlF_6	TiH_2	$CaCO_3$	La	Cr	Graphite	WC
Cu–20Fe-ZTA	50 (80:20)	35	2.5	2.5	3	2	0.5	1	1	2.5
Cu–50Fe-ZTA	50 (50:50)	35	2.5	2.5	3	2	0.5	1	1	2.5
Cu–80Fe-ZTA	50 (20:80)	35	2.5	2.5	3	2	0.5	1	1	2.5

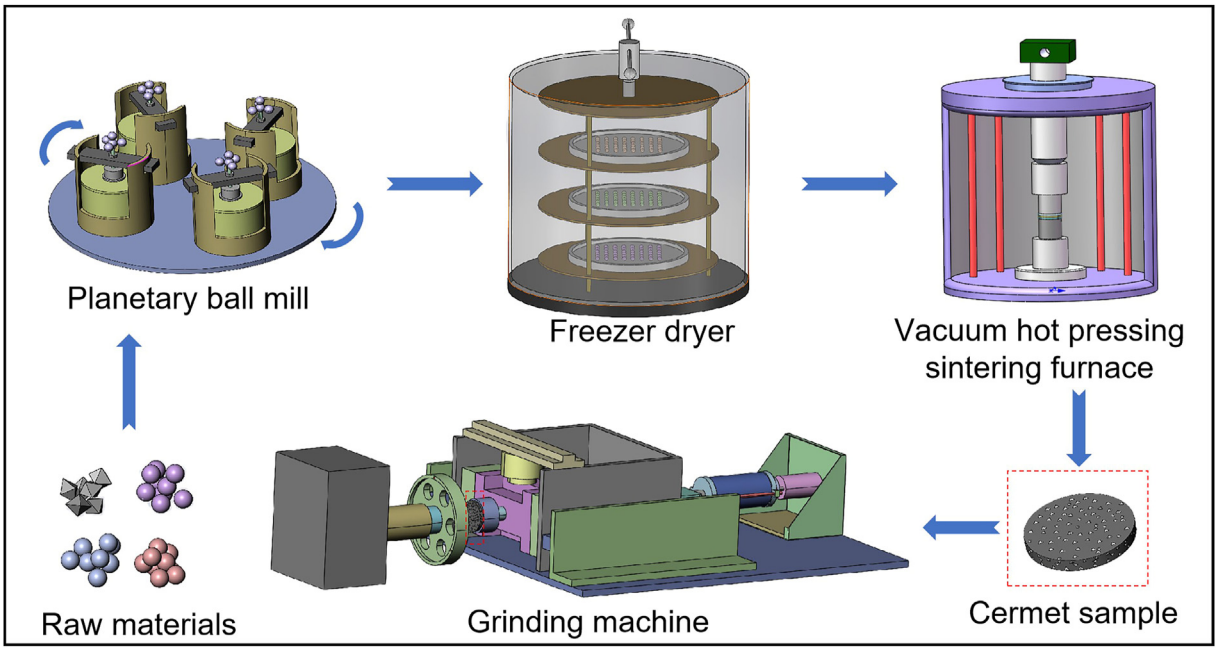

Fig. 1 – Schematic diagram of cermet sample preparation process.

materials (ZTA particles, Cu and Fe binder and other materials) were placed in the ball mill tank of planetary ball mill (WL-1), and tert-butanol was used as the medium to wet grind for 2 h at a speed of 350 r/min. Then the mixed powder slurry was put into freeze-drying machine (FD-A-50) for 24 h to obtain the cermet grinding wheel material powders. Finally, the cermet grinding wheel material was prepared by VHP sintering furnace (VHP-HAS-25). According to the results of pre-experiment, the sintering temperature of the composite powder was set at 1000 °C, the pressure was 12 MPa, and the temperature was kept for 120 min. The process flow chart is shown in Fig. 1.

2.2. *Characterization of samples*

The microstructure of Cu–Fe-ZTA cermet composite powders and bulk materials was examined and analyzed by scanning electron microscopy (SEM), energy dispersive spectroscopy (EDS) and X-ray diffrotometer (XRD). The hardness of Cu–Fe-ZTA cermet was measured by digital micro Vickers hardness tester (HXD-100TM-LCD). The grinding test of rail U71Mn steel was carried out on the grinding test bench (CA6140). The maximum speed of the headstock of the grinding test bench is 1440 r/min. The rail material is machined into a disc with an inner diameter of 244 mm and an outer diameter of 264 mm. The rail material is cut from the rail head and machined into a rail pin with a diameter of 8 mm and a height of 12 mm. After grinding, it can be removed from the rail disc for analysis. The center height of Cu–Fe cermet sample and the rail sample is the same, and the horizontal distance is 15 mm. The grinding test of rail U71Mn steel was carried out on the grinding test bench with the rail speed of 600 r/min and the normal pressure of 500 N applied. During the grinding process, tangential and vertical forces were recorded by LabVIEW (Laboratory Virtual Instrument Engineering Workbench). The more dressing parameters and the grinding parameters are described in detail from our previous work [10]. The most commonly used materials for high-speed railway were used in this study. The chemical composition and physical properties of rail specimen are shown in Table 2. And by white light interference diffrotometer (3D-OM, Contour GT-K, BRUKER), SEM, EDS and X-ray residual stress analyzer (μ-x360n, PULSTEC), the surface morphology of the worn rail specimen and wear debris, surface roughness as well as the residual stress of the rail surface were tested and analyzed respectively. In order to characterize the grinding ability of Cu–Fe-ZTA cermets, the grinding ratio of several cermets to rail specimen was measured.

3. Results and discussion

3.1. *Microstructure analysis of Cu–Fe-ZTA cermets*

Fig. 2 shows the matrix and interface BSE-SEM images of the three prepared Cu–Fe-ZTA cermets. It can be seen from

Table 2 – Chemical composition and physical properties of rail materials.

Chemical composition	Steel bars (wt.%)	C	Si	Mn	S	P	V	Nb
	U71Mn	0.65–0.76	0.15–0.35	1.10–1.40	≤0.03	≤0.03	≤0.03	≤0.010
Physical properties	Steel bars	Tensile strength σ_b (MPa)		Elongation δ (%)		Shrinking rate ψ (%)		Hardness ($HV_{0.05}$)
	U71Mn	≥900		≥10		≥14		290

Fig. 2(a), (d) and (g) that the matrix compositions of the three prepared Cu–Fe-ZTA cermets are different. In Cu–20Fe-ZTA, the white phase occupies the largest area in the matrix. As the main component of the matrix is Cu, EDS results confirm that the white matrix is Cu matrix (point 1), and elements such as Ni and Fe are solidly dissolved in the Cu matrix. Light gray phase also exists in the white matrix phase (point 2), and the light gray phase is dispersed in the Cu matrix. EDS results show that the main components of the light gray phase are Fe, Cr and C, so the light gray phase is Fe based solid solution. Because the solid solubility between Cu and Fe is very small, there is a clear boundary between Cu matrix and Fe solid solution [23]. It can be seen from Fig. 2(d) that the gray phase occupies the largest area in the Cu–50Fe-ZTA cermet matrix. EDS results show that the gray phase is Fe based solid solution, in which elements such as Cu and Cr are solidly dissolved (point 3). The white phase is found around the gray phase, and the EDS results show that the white phase is Cu based solid solution (point 4). Fig. 2(g) shows the BSE-SEM image of Cu–80Fe-ZTA cermet. It can be seen from BSE-SEM image that the phase with the largest area in Cu–80Fe-ZTA cermet matrix is gray phase, and there are white phases at the edge of gray phase. EDS results show that gray and white phases are Fe based solid solution and Cu based solid solution respectively. Gray phase and white phase can be seen in the three cermet matrix due to the same composition of reinforcement phase. EDS results confirm that the bright white phase is WC added to the raw material (point 5), and the dark gray phase is Ti-rich phase (point 8). Combined with previous studies, the dark gray phase is TiO_2 [24]. Fig. 2(b) and (c) shows the BSE-SEM image of the interface between ZTA and matrix of Cu–20Fe-ZTA cermets. It can be seen from the BSE-SEM image that ZTA has a typical stratification phenomenon, and ZTA is composed of white Al_2O_3 and black ZrO_2. It is this special structure that can make ZrO_2 undergo phase transformation from t-ZrO_2 to m-ZrO_2 under stress and make the crack close under tensile load, thus improving toughness [25]. In addition, the interface between ZTA and matrix is well bonded, and no obvious interface is generated, indicating that ZTA and matrix are mechanically bonded. It can also be seen from Fig. 2(e) and (f) that the interface between ZTA particles and the matrix is clear and mechanically bonded, and there are some strengthening phases in the matrix. As can be seen in Fig. 2(i), small black carbides appear in the matrix [26]. Studies have shown that metal Ni can react with Al_2O_3 in

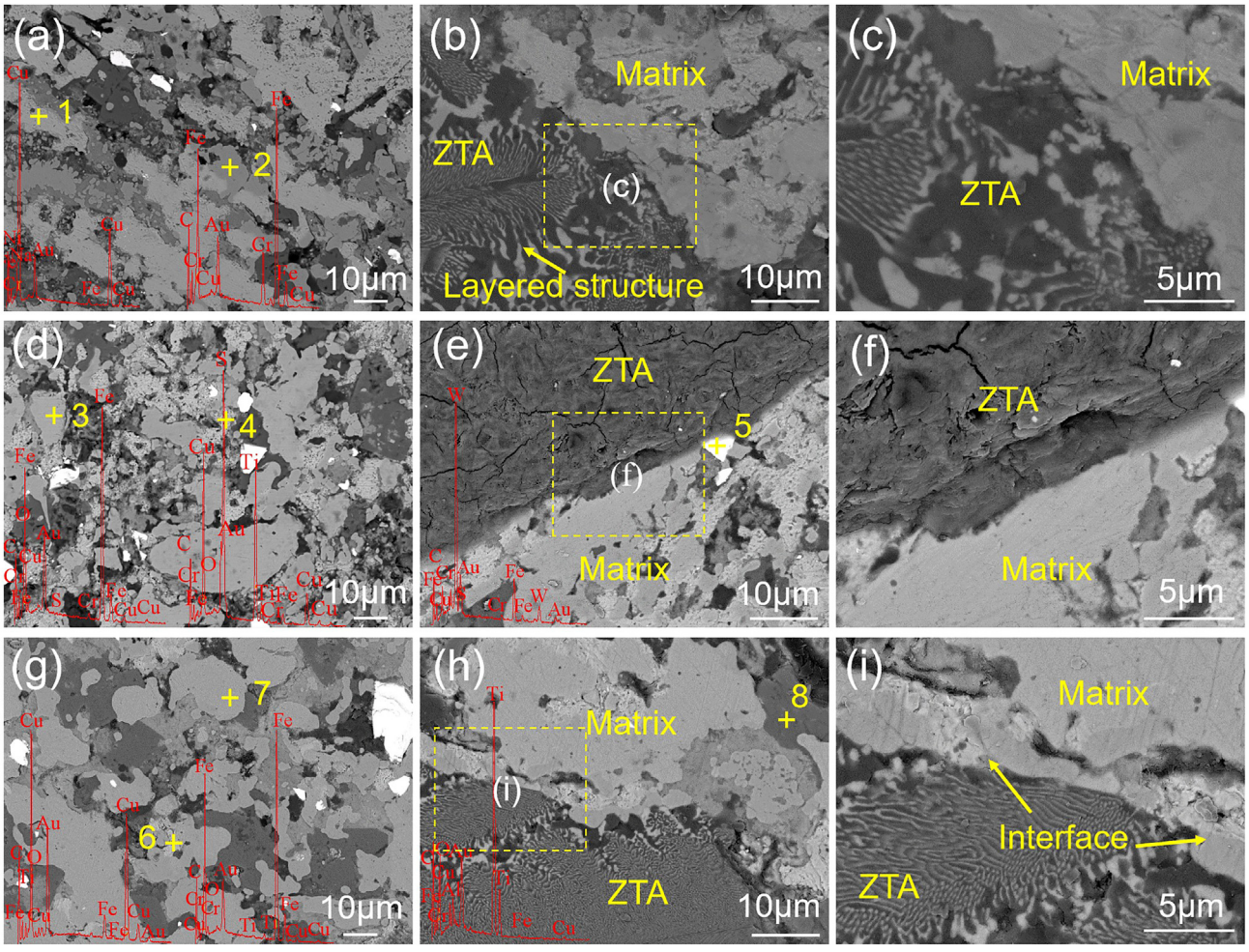

Fig. 2 – Matrix and interface BSE-SEM images of Cu–Fe-ZTA cermets. (a–c) Cu–20Fe-ZTA; (d–f) Cu–50Fe-ZTA; (g–i) Cu–80Fe-ZTA.

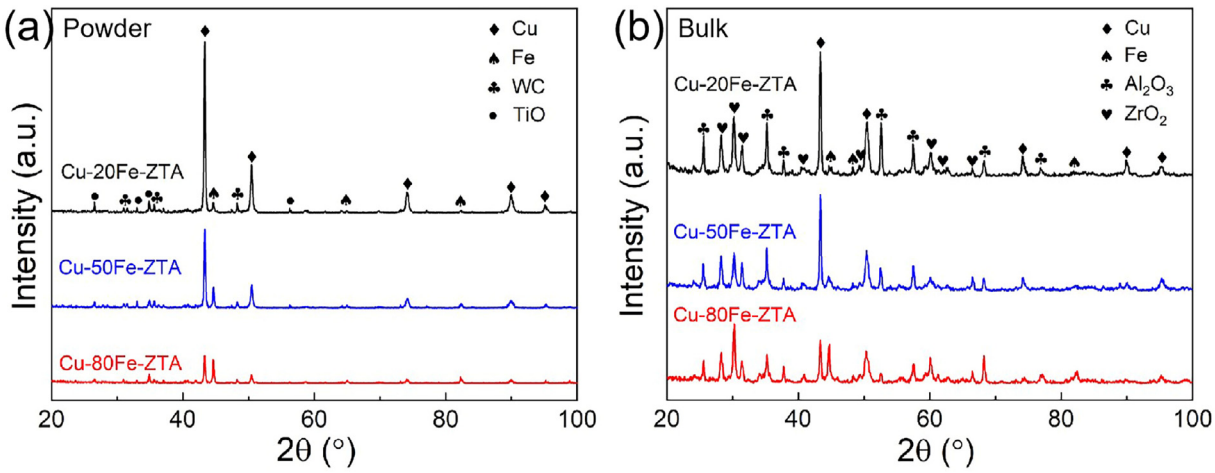

Fig. 3 – XRD results of Cu–Fe-ZTA cermets. (a) powder; (b) bulk.

ZTA to produce Ni aluminate (Al_2NiO_4), under high vacuum and high pressure [27]. The reaction equation is:

$$Al_2O_3 + Ni + O \rightarrow Al_2NiO_4 \quad (1)$$

Meanwhile, from Cu–20Fe-ZTA to Cu–50Fe-ZTA to Cu–80Fe-ZTA, the Fe content increases gradually, while the diffusion rate of Ni into Fe ($D_{Ni\ into\ Fe} = 3.7360 \times 10^{-16}\ m^2/s$) is lower than that of Ni into Cu ($D_{Ni\ into\ Cu} = 10.1946 \times 10^{-16} m^2/s$) [28]. The lower diffusion rate makes more Ni present at the interface, leading to the generation of interface products, so the interfacial layer can be observed in Fig. 2(i). These generated materials moistened the matrix by reaction wetting, and permeated into the depressions and pores on the ceramic surface by capillary force. ZTA particles with uneven surface became relatively uniform, which enhanced the binding ability of ZTA and metal-based binder [8,19].

Fig. 3 shows the XRD results of the prepared Cu–Fe-ZTA cermet powder and bulk. It can be seen from Fig. 3(a) that the phase of the three cermet powders does not change. With the increase of Fe content in cermets, the height of diffraction peak corresponding to Fe increases, while that of Cu decreases, which is consistent with the expected experimental results. XRD results of the powder show peaks of TiO and WC, which may be caused by the decomposition of TiH_2 in the raw material during ball milling. Because of the unstable chemical properties of TiH_2, TiH_2 may be decomposed and oxidized by extrusion or ball milling heat of the powder during grinding. Meanwhile, the decomposed Ti element can improve the wettability between Cu and Al_2O_3 and form Ti_3 $(Cu,Al)_3O$ compound [8,29]. Because the WC added to the matrix has a hexagonal crystal structure, it appears in the XRD results. In addition, other enhancement phases added to the raw material were not detected, probably because the content was below the detection threshold. Fig. 3(b) shows the XRD results of the prepared Cu–Fe-ZTA cermets. It can be seen from the XRD results that the phases of the three prepared cermets are basically the same, which is consistent with the BSE-SEM images results. The diffraction peak height of Fe increases with the increase of Fe content. Theoretically, the diffraction peaks corresponding to Fe elements in Cu–80Fe-ZTA cermets should have a high peak height, but the magnetic elements will affect the XRD results, resulting in low diffraction peaks of Fe and Co elements. Compared with powder XRD results, Al_2O_3 and ZrO_2 peaks appear in bulk XRD results, because ZTA is composed of Al_2O_3 and ZrO_2. Meanwhile, the peaks of TiO and WC disappeared in bulk XRD results. This is because in the sintering process, elements in the raw material diffuse or crystallize into the matrix, and under the cover of the matrix, these elements are lower than the detection threshold and cannot be characterized.

3.2. *Density and hardness test results of Cu–Fe-ZTA cermets*

Archimedes drainage method was used to test the density of Cu–Fe-ZTA cermets, and its density was calculated. The results are shown in Fig. 4. The density of three kinds of Cu–Fe-ZTA cermets prepared in this experiment is 84.6%, 82.4% and 83.9%, respectively. Due to the same ZTA content, the density change of Cu–Fe-ZTA cermets is related to the proportion of Cu and Fe powder. It can be seen from Fig. 4 that when the weight ratio of Cu to Fe is 1:1, the density of cermet is the lowest, and more cracks on ZTA particles are observed in BSE-SEM images (Fig. 2(e)). It is speculated that the solid solubility between Cu and Fe is very low, and greater stress is generated in the sintering process due to the different thermal expansion coefficient between Cu and Fe. Under the action of stress, ZTA near the matrix will undergo phase transformation to release stress [25]. Therefore, cracks appear on the surface of ZTA, which will reduce the density of cermets. When the weight ratio of Cu and Fe powder is changed, the binder with less content in sintering will precipitate along the matrix phase (Fig. 2(a) and (g)), and almost no stress is generated. In addition, the density of cermets is less than 90% for two possible reasons. On the one hand, due to the addition of TiH_2 and $CaCO_3$ in the raw materials, the gas generated by decomposition in the sintering process remains in the matrix, resulting in the reduction of the density of cermet. On the other hand, ZTA is a ceramic phase with many pores inside. In the sintering process, matrix elements such as Cu and Fe are

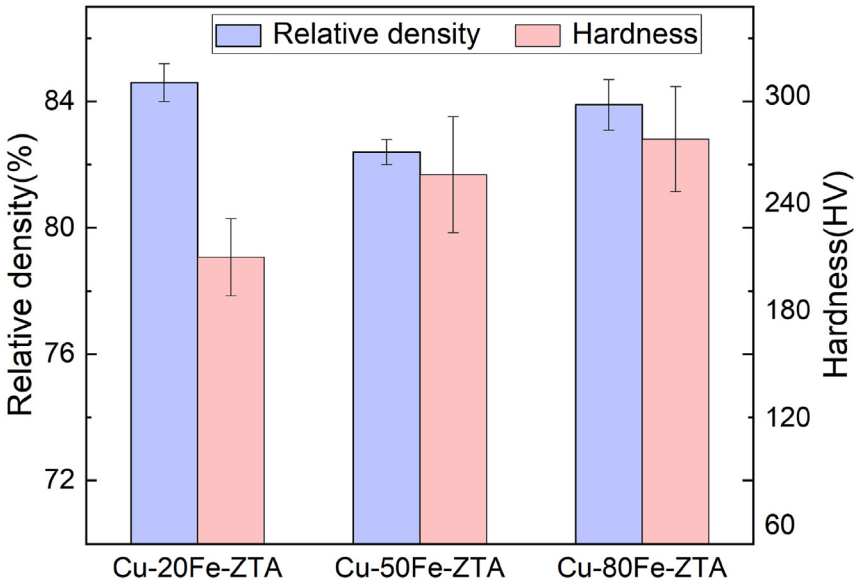

Fig. 4 – Density and microhardness of Cu–Fe-ZTA cermets.

difficult to diffuse into ZTA, so closed pores are formed and the density of the material is reduced. Proper porosity can reduce pre-fatigue caused by grinding, increase heat dissipation, and help to avoid the blockage of cermets [30,31].

The hardness values of the three kinds of Cu–Fe-ZTA cermets prepared in this experiment are shown in Fig. 4. The hardness values of three kinds of Cu–Fe-ZTA cermet are 210.12, 256.23 and 275.98 HV, respectively. The hardness of Cu–Fe-ZTA cermets in this paper are higher than that of Cu-ZTA (192.04 HV) [8]. With the increase of Fe element content in the matrix, the hardness value of cermet increases, because the hardness of Fe matrix is higher than that of Cu matrix. Due to the high porosity of the material, when using the hardness tester to measure the hardness of the sample, the pores cannot bear the pressure well, so the indentation area caused by the indenter is larger, and the hardness value of the cermet also has an impact. WC, graphite and other components added to cermets can refine the grain of materials and increase the hardness of materials to a certain extent [32]. Compared with the hardness of as-cast Cu–10Fe alloy (87 HV) [33], the hardness of cermet sintered by hot pressing is higher, because the cermet sintered by hot pressing has smaller grains than as-cast alloy.

3.3. *Grinding performance of Cu–Fe-ZTA cermets*

The surface morphology of the rail specimens after grinding was analyzed to characterize the grinding effect of cermets. Fig. 5 shows the 3D morphology and 2D profile of rail specimens surface roughness after cermet grinding. It can be seen that the surface roughness of the rail specimens after grinding with Cu–20Fe-ZTA, Cu–50Fe-ZTA and Cu–80Fe-ZTA cermets is 7.972, 13.363 and 22.943 μm, respectively. It can be seen from Fig. 5(a–c) that Cu–20Fe-ZTA cermets have the lowest grinding depth for rail specimens, and their surface roughness is within the range of 10 μm stipulated by railway acceptance standards [34]. With the increase of Fe content in the binder, the grinding depth of Cu–Fe-ZTA cermets on the rail increases, resulting in the increase of rail specimens surface roughness [35]. The hardness results show that the hardness of Cu–80Fe-ZTA cermet matrix is higher than that of the other two cermet samples. In the grinding process, both the abrasive and matrix in cermet are involved in the grinding of the rail specimens. In the grinding process of Cu–20Fe-ZTA cermets, the effective cutting edge of ZTA abrasive breaks along with the grinding process, and the ZTA abrasive after fracture is almost equal to the matrix, so the metal matrix also participates in the grinding. Because the hardness of matrix is softer than that of ZTA abrasive, the metal matrix participates in the grinding of rail specimens in the form of friction. As the grinding process progresses, the metal matrix is expelled from the friction pair, exposing the new ZTA cutting edge, which is repeated during the grinding process. Therefore, Cu–20Fe-ZTA cermets achieve a balance between binder and abrasive. Due to the higher hardness of Cu–50Fe-ZTA matrix, ZTA particles were not peeled off from the matrix in time after being damaged, and these broken particles would have adverse effects on the grinding surface. The hardness of Fe matrix is higher than that of Cu matrix, and the coating ability of Cu–80Fe-ZTA cermets is weak due to the increase of Fe content and decrease of Cu content. In the grinding process, ZTA particles attached to the hard Fe matrix will be pulled out and continue to participate in grinding in the friction pair, resulting in deeper scratches and rougher surfaces.

Fig. 6 shows the friction coefficient and grinding ratio of the three prepared Cu–Fe-ZTA cermets. Since the friction force in the grinding process first increases from 0 to stable stage, the data in the stable stage of friction force is extracted, and the average value of friction value in 1000 cycles is calculated. The stability of friction coefficient represents the balance between normal force and tangential force in the grinding process. As can be seen from Fig. 6, the friction coefficient of cermets increases with the increase of Fe content. Studies show that when the number of cutting units in the middle unit area of

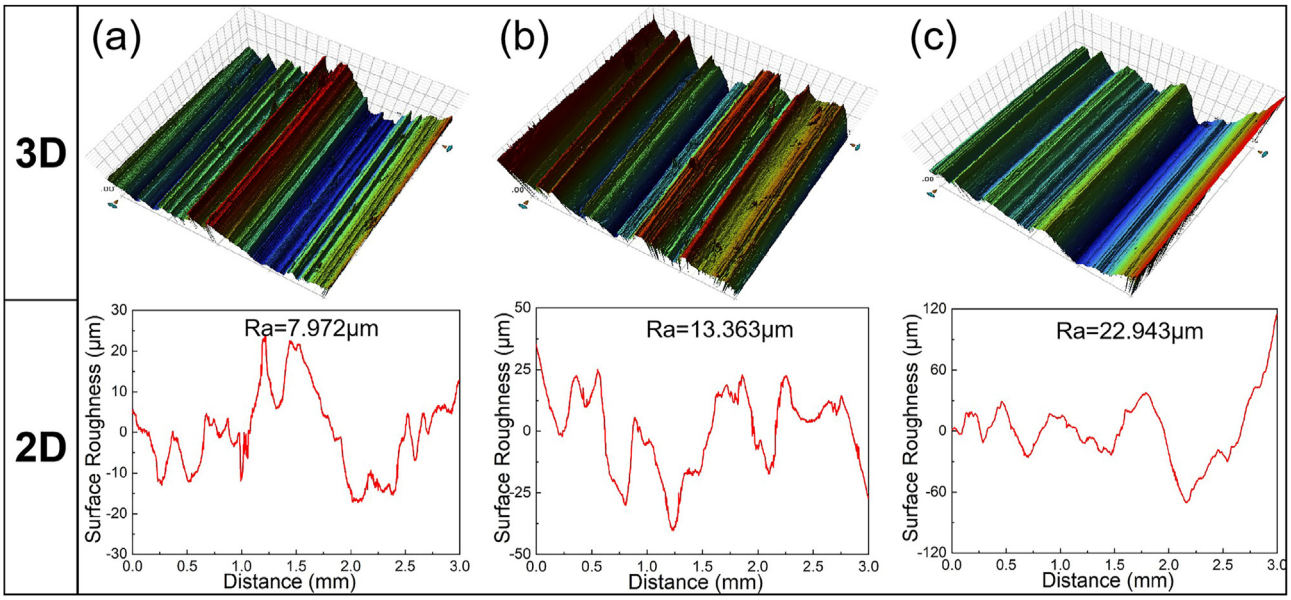

Fig. 5 – 3D morphology and 2D profile of rail specimens surface roughness after cermet grinding. (a) Cu–20Fe-ZTA; (b) Cu–50Fe- ZTA; (c) Cu–80Fe-ZTA.

the friction pair increases, the friction coefficient of the material can be increased [36,37]. Since the prepared Cu–Fe-ZTa cermets have the same ZTA content, the change of friction coefficient is related to the proportion of Cu–Fe binder. The hardness of cermet matrix increases with the increase of Fe content in the binder. In the grinding process, the hard Fe matrix is broken into the friction pair to participate in grinding, and the fine Fe binder produces furrowing scratches on the rail surface with the grinding process, and finally the friction pair is discharged under the action of tangential force. In the Cu–20Fe-ZTA cermet, due to the higher Cu content, the friction and wear between the soft Cu matrix and the rail occur in the grinding process, so the grinding amount is less. This result is consistent with the minimum roughness obtained by 3D morphology of rail surface roughness.

The results of grinding ratio of Cu–Fe-ZTA cermets show that the highest grinding ratio of Cu–50Fe-ZTA cermet is 71.96, and the lowest grinding ratio of Cu–80Fe-ZTA cermet is 32.62. As the grinding ratio is the ratio of the material amount of the workpiece to the amount of cermets wear, the cermets have greater wear after grinding with Cu–80Fe-ZTA cermet, so the grinding is lower. In the matrix of Cu–20Fe-ZTA cermet, the Cu matrix with good ductility always participates in the grinding process in the way of friction and wear, so the grinding amount of the workpiece and the wear amount of cermets are lower, so the grinding ratio is lower than that of Cu–50Fe-ZTA cermet. The grinding effect of Cu–50Fe-ZTA cermet is the best. The possible reason is that the hardness of Cu–50Fe-ZTA cermet matrix is high, the matrix is not easy to fracture in the grinding process, ZTA abrasive damage did not

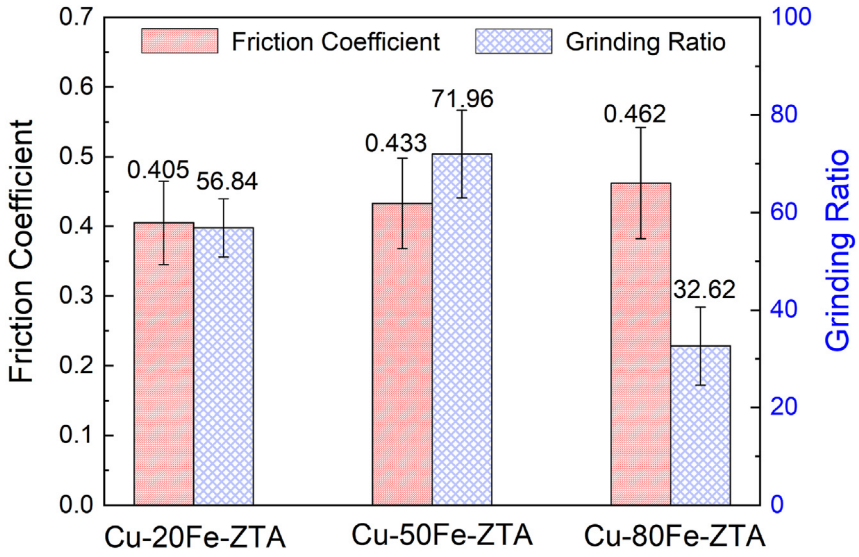

Fig. 6 – Friction coefficient and grinding ratio of cermets.

peel in time, will continue to participate in the grinding process. Although the hardness is lower than Cu–80Fe-ZTA cermet, but because of the low wear of cermets, so the grinding is relatively high.

Residual stress is one of the most important factors to evaluate the surface integrity, and its uneven distribution will shorten the service life of rail greatly. Fig. 7 shows the compressive residual stress diagram of the rail surface after grinding with Cu–Fe-ZTA cermets. Due to the plastic deformation and grinding heat of the rail during grinding, residual stress exists on the surface of the rail [38]. Because the plastic deformation direction of the rail is different, the residual stress value of the rail is different in each direction after grinding. The residual stress parallel to the grinding direction (σ_x) is higher and the residual stress perpendicular to the grinding direction (σ_y) is lower due to the larger deformation of the rail parallel to the grinding direction. According to the above analysis, in the grinding process, the rail is squeezed by the abrasive, and the rail material flows along both sides of the abrasive under the action of tangential force, resulting in scratches on the rail surface. Because the rail material is extruded outward, there is residual compressive stress perpendicular to the grinding direction. After grinding with Cu–20Fe-ZTA cermets, due to the soft Cu matrix, the effective cutting edge of Cu–20Fe-ZTA cermets in the grinding process is broken. The friction between cermets and rail occurs, the plastic deformation degree of rail surface is small, and the grinding amount of cermets to rail is also low. The residual stress parallel to the grinding direction is 180.5 MPa, and the residual stress perpendicular to the grinding direction is 89.6 MPa. When the Fe content in cermet matrix increases, the hardness value of cermet matrix increases, and the grinding mode of cermet on rail changes from friction to ploughing and cutting. The cumulative thermoplastic deformation of metal materials is characterized by the increase of residual compressive stress due to the plow and cutting effects of abrasive [39]. The plastic deformation degree of the rail surface after grinding with Cu–50Fe-ZTA and Cu–80Fe-ZTA cermets is relatively high. The cutting amount of cermets on the rail increases, and the rail surface becomes rougher, so the residual stress value is relatively high. The residual stresses parallel to the grinding direction are 260.5 and 456.1 MPa, and the residual stresses perpendicular to the grinding direction are 119.9 and 325.6 MPa, respectively.

The material removal mechanism can be revealed by studying the debris generated in the grinding process. Fig. 9 shows the SEM image of the grinding debris of the prepared Cu–Fe-ZTA cermets. Generally, the morphology of debris is divided into flaky debris, spherical debris and curled debris. It can be seen from Fig. 8(a–c) that flaky, spherical and curled debris are produced after grinding with Cu–20Fe-ZTA cermet. Flaky debris is the most common form of grinding debris. When the rail surface is subjected to a large load, the material on the rail surface compresses and flows forward along the direction of friction. This could be the reason why flaky debris is the most common form of grinding debris. In the grinding process, due to the action of grinding heat, the thin debris are easy to oxidize or melt and form spherical debris [31]. The flaky and spherical debris indicate that the grinding mechanism of Cu–20Fe-ZTA cermet is friction and wear. In Fig. 8(c), curled debris can be seen. These grinding debris are caused by the abrasive being pressed into the rail surface during the

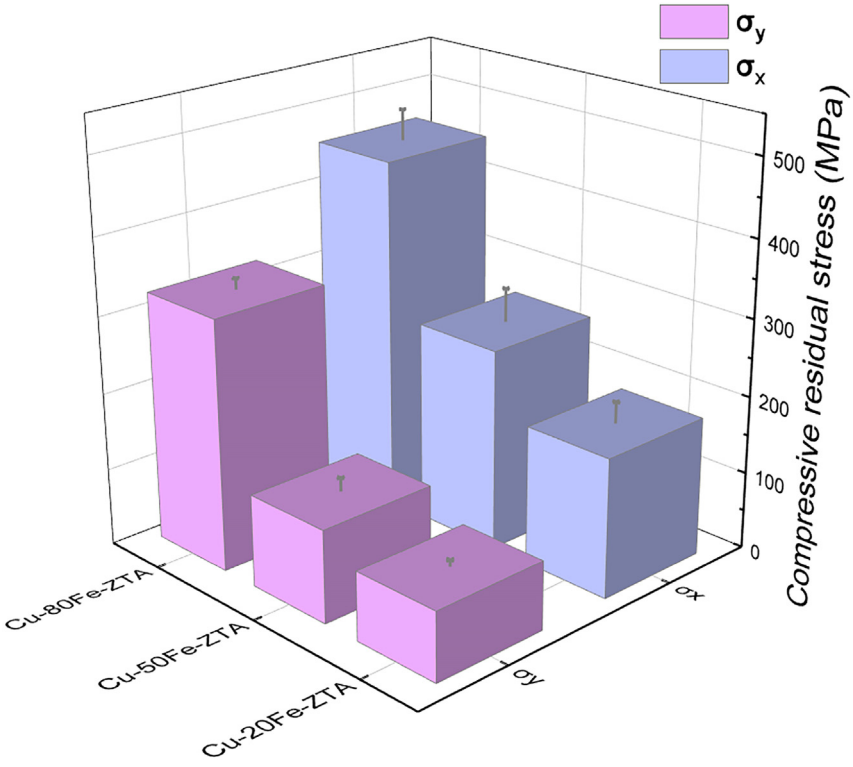

Fig. 7 – Residual stress on rail surface after cermet grinding.

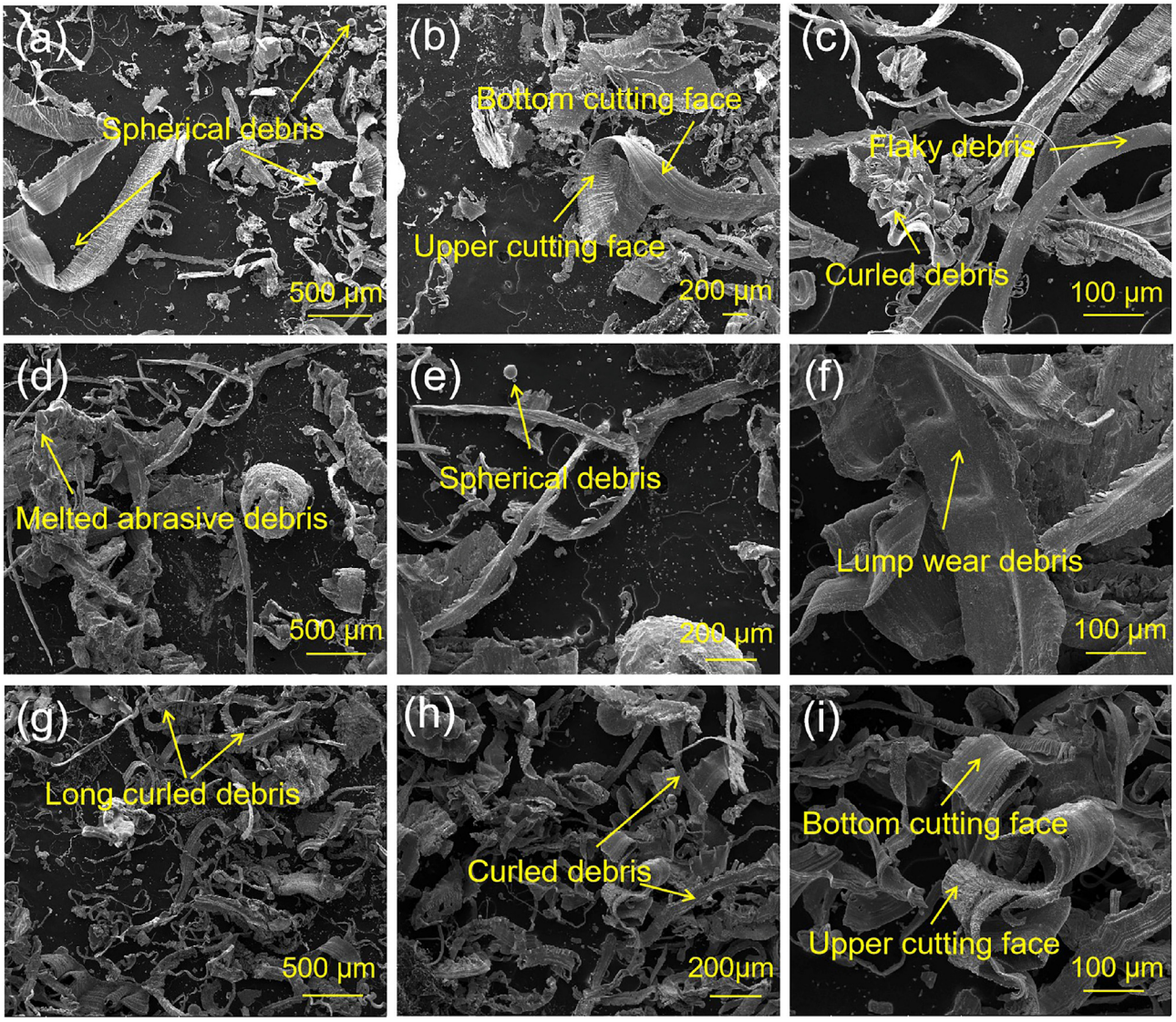

Fig. 8 – SEM image of grinding debris of Cu–Fe-ZTA cermet after grinding. (a–c) Cu–20Fe-ZTA; (d–f) Cu–50Fe-ZTA; (g–i) Cu–80Fe-ZTA.

grinding process, and the sharp cutting edge has a cutting effect on the rail under the action of tangential force, forming curled debris [40]. Fig. 8(d–f) is a image of grinding debris produced by using Cu–50Fe-ZTA cermet, from which we can see spherical, flaky and melted debris. As can be seen from the above, the grinding ratio of Cu–50Fe-ZTA cermet grinding is high, so a large number of massive gringding debris are produced in the grinding process. At the same time, a lot of grinding heat is generated during grinding. And the debris melt and intertwine with each other under the influence of grinding heat, resulting in lump melted debris and spherical debris. Due to the control effect of Fe matrix on abrasive in Cu–50Fe-ZTA cermets, the broken cutting edge does not peel off and continues to participate in the grinding process. And the contact area between the broken cutting edge and rail increases, resulting in wider massive grinding debris [41]. With the increase of Fe content in cermet, the morphology of grinding debris changes after grinding rail specimens. It can be seen from Fig. 8(g–i) that the morphology of the grinding debris produced after Cu–80Fe-ZTA cermet grinding rail is almost all curled debris. As can be seen from Fig. 8(i), the bottom cutting surface is characterized by smooth structure, while the upper cutting surface is characterized by folds or serrations, namely the so-called free surface [42]. The formation of curled debris is caused by the plastic accumulation of the rail specimen along the cutting direction after the abrasive is pressed into the surface [43], and two conditions need to be met for its formation. First, the negative front angle between abrasive and rail in cermets is small. Second, abrasive self sharpness is strong. The abrasive used in this paper is ZTA, which has strong self-sharpening. But in comparison, the wettability of Fe and ZTA is worse, so the coating ability of Cu–80Fe-ZTA cermets in the grinding process is weak. It is likely to cause loss or abrasive fracture. Abrasive fracture can produce new cutting edge to participate in the grinding of abrasive. Falling abrasive residues produce deeper but sparser

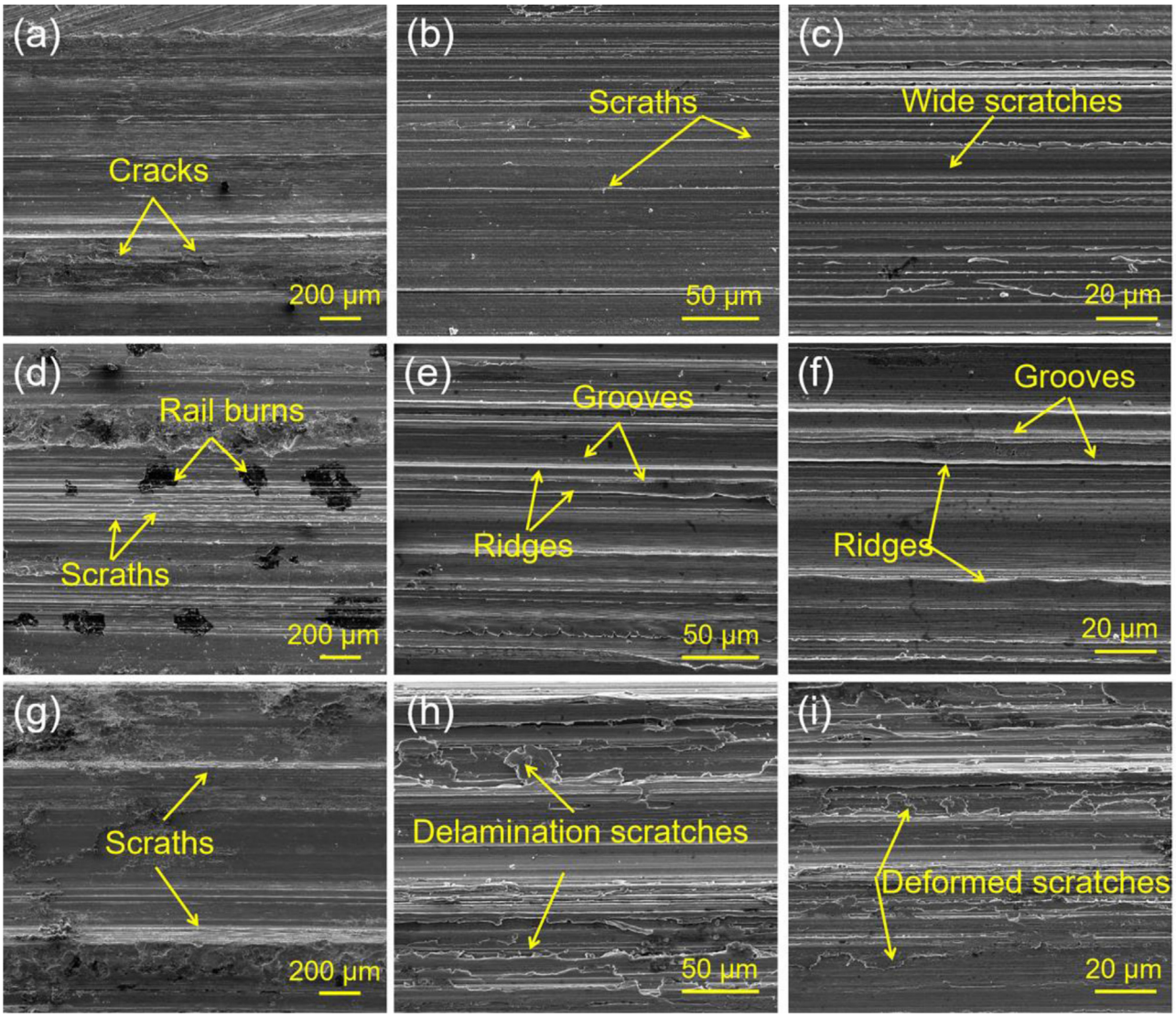

Fig. 9 – Surface morphology of rail specimens after grinding. (a–c) Cu–20Fe-ZTA; (d–f) Cu–50Fe-ZTA; (g–i) Cu–80Fe-ZTA.

scratches in the friction pair. The resulting plastic accumulation displaces friction pairs during grinding and forms curled debris.

Fig. 9 shows the SEM morphology of the rail surface after grinding three kinds of cermets. The grinding process is divided into friction, ploughing and cutting according to the way the abrasive removes the rail material [44]. It can be seen from Fig. 9(a–c) that the rail specimens surface is relatively smooth after grinding with Cu–20Fe-ZTA cermet, and cracks exist in some areas (Fig. 9(a)). These cracks expand along the rail surface in the subsequent grinding process, and finally cause the rail surface to flake, and the spalling rail material displaces the friction pair in the form of wear debris. Due to the high grinding heat, the material on the rail surface is softened and tends to form wide grooves, as shown in Fig. 9(c). The grinding mechanism of cermets changes from friction to ploughing and cutting when Fe binder content increases. It can be seen from Fig. 9(d) that the grinding surface of material surface after Cu–50Fe-ZTA cermets grinding is relatively smooth and the surface undulation of rail is low, which is consistent with the result of 2D profile in Fig. 5(b). In addition, there were more burns on the rail surface. It can be seen from Fig. 9(e) that there are high grinding ridges on the surface of the rail, and grooves exist on both sides of the grinding ridges, which is the result of the extrusion of the abrasive on the rail surface [45]. When the cutting depth exceeds the critical value, debris are formed and the material accumulates on both sides of the groove that forms a plastic heave [46,47]. There are wide scratches in Fig. 9(f), and the grinding surface is relatively smooth. This is because during the grinding process, the binder can coat the ZTA abrasive, which grinds continuously during the grinding process to form a relatively flat grinding surface. When Fe content continues to increase, the grinding effect of Cu–80Fe-ZTA cermets on rail is further increased. It can be seen from Fig. 9(g–i) that deep grooves and delamination scratches occur on the rail surface after Cu–80Fe-ZTA cermets are ground. Delamination scratches may be caused by the deep grooves caused by the relative sliding and repeated

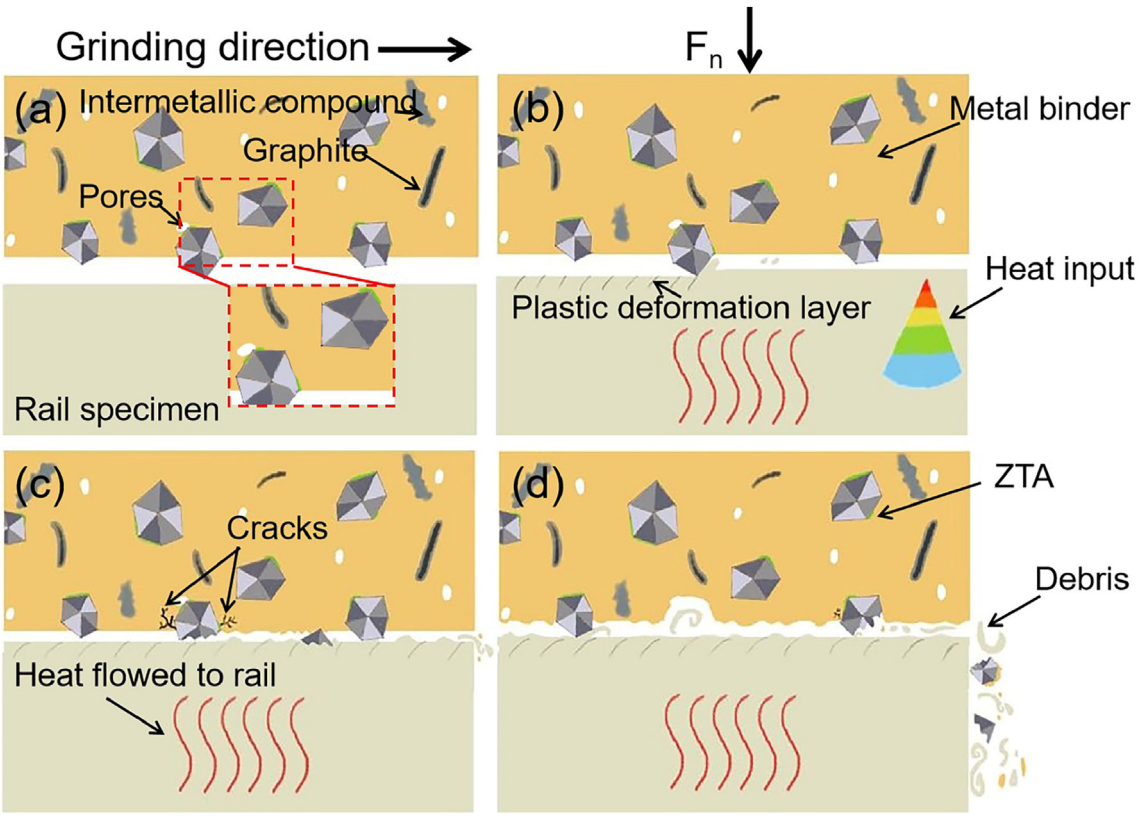

Fig. 10 – Schematic diagram of cermet grinding on the surface of rail specimen. (a) Original state; (b-c) Ploughing and cutting processes; (d) Self sharpening of Cu–Fe-ZTA.

extrusion between the exfoliated ZTA abrasive and the rail in the friction pair during grinding [31]. The existence of delamination scratches leads to the increase of longitudinal wave height of rail surface and the increase of surface roughness of rail, which also confirms the results of the worst surface quality of rail after Cu–80Fe-ZTA cermet grinding.

3.4. *Interface formation and wear mechanism of cermet*

The wear behavior of Cu–Fe-ZTA in grinding process can be better revealed by studying the binding interface between matrix and ZTA. In the above analysis, it can be known that there are mechanical bonding and reactive bonding interfaces between ZTA and matrix. The metal particles deform and melt under high temperature and load conditions, and the melted liquid phase fills the gap between ZTA and the matrix. At the same time, after atomic substitution, Ni atoms on the surface of ZTA will diffuse into the matrix and form solid solution with Cu and Fe, thus increasing the strength of the matrix. The vacancy formed by the diffusion of Ni atoms will also be filled by metal atoms in the matrix. In addition, Al_2O_3 in ZTA particles reacts with Ti and Cu in the matrix to form compounds, forming reaction bonding interfaces [8]. Whereas, due to the low Ni content, there are fewer interfaces for reaction bonding as shown in Fig. 10(a).

It is important to study the wear mechanism of cermets in industrial production process. As is known to all, the wear properties of cermets are mainly affected by matrix hardness, binder bonding ability and abrasive type [48,49]. Abrasive and binder wear continuously during the grinding process, and about 80% of the energy is transferred to the rail specimen and cermet in the form of heat. Certain pore structures in cermet help to dissipate heat [31,50]. Under loading conditions, ZTA particles contact the surface of the reinforcement bar, as shown in Fig. 10(b). Under the action of tangential force, ZTA particles will undergo abrasive wear. When the tangential force exceeds the shear toughness of the abrasive, the ZTA particles gradually break and form a new sharp edge, as shown in Fig. 10(c). When the tangent force exceeds the abrasive holding force, the porous interface layer ruptures due to increased load, resulting in the extraction of ZTA particles, as shown in Fig. 10(d). The particle pull-out phenomenon is mainly caused by bond fracture or bond interface fracture [51]. In addition, when all the protruding ZTA particles are worn parallel to the matrix, or some ZTA particles are pulled out during the grinding process, the matrix adhesive directly contacts the rail and takes part in the grinding process and remains on the surface of the rail [30,51]. When the matrix is soft and easy to wear, the new ZTA abrasive particles are exposed on the cermet surface. If the matrix is hard and the coating ability is poor (such as Cu–80Fe-ZTA), the ZTA particles will remain between the friction pairs, resulting in grooves and deep grinding grooves in the grinding process.

4. Conclusion

In this paper, Cu-xFe-ZTA (x = 20, 50, 80) with different binder ratios were prepared by powder metallurgy method. The conclusions obtained are as follows:

(1) Cu-xFe-ZTA cermet has good compactness after VHP sintering, and the addition of alloying elements plays a role of solution strengthening. Since ZTA reacts with Ni element in matrix to form Ni aluminate (Al_2NiO_4), there are both mechanical and reactive bonding interfaces at the interface of Cu–Fe-ZTA.
(2) In conclusion, Cu–20Fe-ZTA cermets have the best grinding effect, with a friction coefficient of 0.405 and a surface roughness of 7.972 μm. And its residual stress distribution is relatively uniform. The difference of cermet grinding performance lies in the binding force between metal matrix and abrasive. When the content of Cu in the matrix is high, the coating ability of abrasive is strong. But the matrix is soft and easy to wear, so the cermet has strong self-sharpening, Cu–20Fe-ZTA grinding effect is the best.
(3) The failure of Cu–Fe-ZTA cermets is mainly due to the difference of coating effect of Cu-xFe binder on ZTA cermets. During loading, ZTA wear, fracture and pull-out occur at Cu–Fe binder/ZTA interface, resulting in failure.

Data availability

The data used to support the findings of this study are available from the corresponding author upon request.

Declaration of Competing Interest

The authors declare that they have no known competing financial interests or personal relationships that could have appeared to influence the work reported in this paper.

Acknowledgments

This work was supported by Key Laboratory of Infrared Imaging Materials and Detectors, Shanghai Institute of Technical Physics, Chinese Academy of Sciences (No. IIMDKFJJ-21-10), China Postdoctoral Science Foundation (No. 2018T110993).

REFERENCES

[1] Zhou ZF, Shan Q, Jiang YH, Li ZL, Zhang ZX. Effect of nanoscale V2C precipitates on the three-body abrasive wear behavior of high-Mn austenitic steel. Wear 2019;436–437. 203009, https://doi.org/10.1016/j.wear.2019.203009.
[2] Feldshtein EE, Dyachkova LN, Krolczykc GM. On the evaluation of certain strength characteristics and fracture features of iron-based sintered MMCs with nanooxide additives. Mater Sci Eng A-Struct 2019;756:455–63. https://doi.org/10.1016/j.msea.2019.04.044.
[3] Yang RS, Cao SH, Kang WX, Li JL, Jiang XY. Mechanism analysis of spalling defect on rail surface under rolling contact conditions. Math Probl Eng 2018;2018:7012710. https://doi.org/10.1155/2018/7012710.
[4] Cantini S, Cervello S. The competitive role of wear and RCF: full scale experimental assessment of artificial and natural defects in railway wheel treads. Wear 2016;366–367:325–37. https://doi.org/10.1016/j.wear.2016.06.020.
[5] Liu JP, Zhou QY, Zhang YH, Liu FS, Tian CH, Li C, et al. The formation of martensite during the propagation of fatigue cracks in pearlitic rail steel. Mat Sci Eng A-Struct 2019;747:199–205. https://doi.org/10.1016/j.msea.2019.01.049.
[6] Haidemenopoulos GN, Sarafoglou PI, Christopoulos P, Zervaki AD. Rolling contact fatigue cracking in rails subjected to in-service loading. Fatigue Fract Eng M 2016;39:1161–72. https://doi.org/10.1111/ffe.12432.
[7] Feng Q, Duan XZ, Dong BX, Yang HY, Lu JB, Li XJ. Effects of Cr and Zr addition on microstructures, compressive properties, and abrasive wear behaviors of in situ TiB2/Cu cermets. Materials 2018;11(8):1464. https://doi.org/10.3390/ma11081464.
[8] Sun DM, Jiang XS, Sun HL, Song TF, Luo ZP. Microstructure and mechanical properties of Cu-ZTA cermet prepared by vacuum hot pressing sintering. Mater Res Exp 2020;7:026530. https://doi.org/10.1088/2053-1591/ab6c19.
[9] Gu KK, Lin Q, Wang WJ, Wang HY, Guo J, Liu QY, et al. Analysis on the effects of rotational speed of grinding stone on removal behavior of rail material. Wear 2015;342–343:52–9. https://doi.org/10.1016/j.wear.2015.08.008.
[10] Sun DM, Jiang XS, Sun HL, Fang YJ, Song TF. Effect of SiCP content on the microstructure and mechanical properties of Fe-based cermets. Int J Adv Manuf Technol 2022;118:2539–57. https://doi.org/10.1007/s00170-021-08101-3.
[11] Chatterjee A, Sprague E, Mazumder J, Misra A. Hierarchical microstructures and deformation behavior of laser direct-metal-deposited Cu-Fe alloys. Mater Sci Eng A 2021;802:140659. https://doi.org/10.1016/j.msea.2020.140659.
[12] Abbas SF, Park KT, Kim TS. Effect of composition and powder size on magnetic properties of rapidly solidified copper-iron alloys. J Alloys Compd 2018;741:1188–95. https://doi.org/10.1016/j.jallcom.2018.01.245.
[13] Zhang P, Yuan XB, Li YD, Zhou YH, Lai RL, Li YP, et al. Influence of minor Ag addition on the microstructure and properties of powder metallurgy Cu-10 wt% Fe alloy. J Alloys Compd 2022;904:163983. https://doi.org/10.1016/j.jallcom.2022.163983.
[14] Li WS, Zhang J, Dong HF, Chu K, Wang SC, Liu Y, et al. Thermodynamic and kinetic study on interfacial reaction and diamond graphitization of Cu-Fe-based diamond composite. Chinese Phys B 2013;22:018102. https://doi.org/10.1088/1674-1056/22/1/018102.
[15] Naga SM, El-Maghraby HF, Elgamhoudy M, Saleh MA. Characterization and origin of failure of SiC/ZTA composites. Int J Refract Met H 2018;73:53–7. https://doi.org/10.1016/j.ijrmhm.2018.01.016.
[16] Mamivand M, Asle ZM, Kadiri HE. Phase field modeling of stress-induced tetragonal-to-monoclinic transformation in zirconia and its effect on transformation toughening. Acta Mater 2014;64:208–19. https://doi.org/10.1016/j.actamat.2013.10.031.
[17] Sui YD, Zhou MJ, Jiang YH. Characterization of interfacial layer of ZTA ceramic particles reinforced iron matrix composites. J Alloy Compd 2018;741:1169–74. https://doi.org/10.1016/j.jallcom.2018.01.199.

[18] Pfeifer S, Demirci P, Duran R, Stolpmann H, Renfftlen A, Nemrava S, et al. Synthesis of zirconia toughened alumina(ZTA) fibers for high performance materials. J Eur Ceram Soc 2016;36(3):725–31. https://doi.org/10.1016/j.jeurceramsoc.2015.10.028.
[19] Ru JJ, He H, Jiang YH, Zhou R, Hua YX. Wettability and interaction mechanism for Ni-modified ZTA particles reinforced iron matrix composites. J Alloy Compd 2019;786:321–9. https://doi.org/10.1016/j.jallcom.2019.01.342.
[20] Fan L, Wang Q, Yang P, Chen HH, Hong HP, Zhang WT. Preparation of nickel coating on ZTA particles by electroless plating. Ceram Int 2018;44(10):11013–21. https://doi.org/10.1016/j.ceramint.2018.03.055.
[21] Mohammadmehdi S, Mohammad HP, Reza Z, Maryam G, Mohammad MM. Microstructural and sliding wear behavior of SiC-particle reinforced copper matrix composites fabricated by sintering and sinter-forging processes. J Mater Res Technol 2016;5(1):5–12. https://doi.org/10.1016/j.jmrt.2015.03.002.
[22] Ji WB, Zou B, Huang CZ, Liu YN, Huang CM. Fabrication, microstructure and mechanical properties of self-diffusion gradient cermet composite tool materials. Mater Sci Eng A-Struct 2017;685:332–41. https://doi.org/10.1016/j.msea.2017.01.028.
[23] Shen YJ, Mi ST, Sun L, Yang LY, Gong HR. Mechanical properties and dislocation evolution of Cu-Fe interfaces from molecular dynamic simulation. Mater Chem Phys 2021;261:124270. https://doi.org/10.1016/j.matchemphys.2021.124270.
[24] Joshua P. Reactions in the matrix and interface of the Fe-SiC metal matrix composite system. Mater Sci Eng A-Struct 1999;269(1–2):225–41. https://doi.org/10.1016/S0921-5093(99)00158-6.
[25] Mahmood M, Mohsen AZ, Haitham EK. Phase field modeling of stress-induced tetragonal-to-monoclinic transformation in zirconia and its effect on transformation toughening. Acta Mater 2014;64:208–19. https://doi.org/10.1016/j.actamat.2013.10.031.
[26] Sun DM, Jiang XS, Sun HL, Song TF, Luo ZP. Microstructure and mechanical properties of Fe-ZTA cermet prepared by vacuum hot-pressed sintering. Mater Res Exp 2020;7:026518. https://doi.org/10.1088/2053-1591/ab70e4.
[27] Yin ZB, Yan SY, Xu WW, Yuan JT. Microwave sintering of Ti(C, N)-based cermet cutting tool material. Ceram Int 2018;44(1):1034–40. https://doi.org/10.1016/j.ceramint.2017.10.041.
[28] Gao Q, Jiang XS, Sun HL, Song TF, Mo DF, Li X. Interfacial reaction and microstructure investigation of 4J36/Ni/Cu/V/TC4 diffusion-bonded joints. Mater Lett 2021;305:130809. https://doi.org/10.1016/j.matlet.2021.130809.
[29] Voytovych R, Robaut F, Eustathopoulos N. The relation between wetting and interfacial chemistry in the CuAgTi/alumina system. Acta Mater 2006;54(8):2205–14. https://doi.org/10.1016/j.actamat.2005.11.048.
[30] Zhang WL, Liu CB, Yuan YJ, Zhang PF, Fan XQ. Probing the effect of abrasive wear on the grinding performance of rail grinding stones. J Manuf Process 2021;64:493–507. https://doi.org/10.1016/j.jmapro.2021.02.014.
[31] Yuan YJ, Zhang WL, Zhang PF, Fan XQ, Zhu MH. Porous grinding wheels toward alleviating the pre-fatigue and increasing the material removal efficiency for rail grinding. Tribol Int 2021;154:106692. https://doi.org/10.1016/j.triboint.2020.106692.
[32] Bradbury CR, Gomon JK, Kollo L, Kwon H, Leparoux M. Hardness of multi wall carbon nanotubes reinforced aluminium matrix composites. J Alloys Compd 2014;585:362–7. https://doi.org/10.1016/j.jallcom.2013.09.142.
[33] Wang M, Jiang YB, Li Z, Xiao Z, Gong S, Qiu WT. Microstructure evolution and deformation behaviour of Cu-10 wt%Fe alloy during cold rolling. Mater Sci Eng A-Struct 2021;801(9):140379. https://doi.org/10.1016/j.msea.2020.140379.
[34] Standard EN 13231-3. Railway applications-track-acceptance of works-Part 3: acceptance of reprofiling rails in track. 2012.
[35] Zhou K, Ding HH, Wang WJ, Wang RX, Liu QY. Influence of grinding pressure on removal behaviours of rail material. Tribol Int 2019;134:417–26. https://doi.org/10.1016/j.triboint.2019.02.004.
[36] Yang ZC, Zhu LD, Lin B, Zhang GX, Ni CB, Sui TY. The grinding force modeling and experimental study of ZrO_2 ceramic materials in ultrasonic vibration assisted grinding. Ceram Int 2019;45(7):8873–89. https://doi.org/10.1016/j.ceramint.2019.01.216.
[37] Zhou K, Ding HH, Zhang SY, Guo J, Liu QY, Wang WJ. Modelling and simulation of the grinding force in rail grinding that considers the swing angle of the grinding stone. Tribol Int 2019;137:274–88. https://doi.org/10.1016/j.triboint.2019.05.012.
[38] Chen X, Rowe WB, McCormack DF. Analysis of the transitional temperature for tensile residual stress in grinding. J Mater Process Tech 2000;107(1–3):216–21. https://doi.org/10.1016/s0924-0136(00)00692-0.
[39] Mahdi M, Zhang L. Applied mechanics in grinding-VI. Residual stresses and surface hardening by coupled thermo-plasticity and phase transformation. Int J Mach Tool Manuf 1998;38:1289–304. https://doi.org/10.1016/S0890-6955(97)00134-X.
[40] Denkena B, Köhler J, Kästner J. Chip formation in grinding: an experimental study. Prod Eng 2012;6(2):107–15. https://doi.org/10.1007/s11740-011-0360-8.
[41] Malkin S. Grinding technology: theory and applications of machining with abrasives. Int J Mach Tool Manu 1991;31(3):435–6. https://doi.org/10.1016/0890-6955(91)90088-K.
[42] Cai M, Gong YD, Sun Y, Qu SS, Liu Y, Yang YY. Experimental study on grinding surface properties of nickel-based single crystal superalloy DD5. Int J Adv Manuf Tech 2019;101:71–85. https://doi.org/10.1007/s00170-018-2839-3.
[43] Zhang WL, Zhang PF, Zhang J, Fan XQ, Zhu MH. Probing the effect of abrasive grit size on rail grinding behaviors. J Manuf Processes 2020;53:388–95. https://doi.org/10.1016/j.jmapro.2020.03.028.
[44] Zhou N, Peng RL, Pettersson R. Surface integrity of 2304 duplex stainless steel after different grinding operations. J Mater Process Tech 2016;229:294–304. https://doi.org/10.1016/j.jmatprotec.2015.09.031.
[45] Zhang PF, Zhang WL, Yuan YJ, Fan XQ, Zhu MH. Probing the effect of grinding-heat on material removal mechanism of rail grinding. Tribol Int 2020;147:105942. https://doi.org/10.1016/j.triboint.2019.105942.
[46] Zhang YB, Li CH, Ji HJ, Yang XH, Yang M, Jia DZ. Analysis of grinding mechanics and improved predictive force model based on material-removal and plastic-stacking mechanisms. Int J Mach Tool Manu 2017;122:81–97. https://doi.org/10.1016/j.ijmachtools.2017.06.002.
[47] Yang M, Li CH, Zhang YB, Jia DZ, Zhang XP, Hou YL. Maximum undeformed equivalent chip thickness for ductile-brittle transition of zirconia ceramics under different lubrication conditions. Int J Mach Tool Manu 2017;122:55–65. https://doi.org/10.1016/j.ijmachtools.2017.06.003.
[48] Li Q, Li ZH, Tan HY, Feng DD, Zhu YM. Comparison of Cu and Zn on properties of vitrified diamond composites. Diam Relat Mater 2016;66:217–22. https://doi.org/10.1016/j.diamond.2016.05.008.

[49] Miao Q, Ding WF, Fu DK, Chen ZZ, Fu YC. Influence of graphite addition on bonding properties of abrasive layer of metal-bonded CBN wheel. Int J Adv Manuf Tech 2017;93:2675–84. https://doi.org/10.1007/s00170-017-0714-2.
[50] Wang YG, Li CH, Zhang YB, Li BK, Yang M, Zhang XP. Experimental evaluation of the lubrication properties of the wheel/workpiece interface in MQL grinding with different nanofluids. Tribol Int 2016;99:198–210. https://doi.org/10.1016/j.triboint.2016.03.023.
[51] Li Z, Ding WF, Ma CY, Xu JH. Grinding temperature and wheel wear of porous metal-bonded cubic boron nitride superabrasive wheels in high-efficiency deep grinding. P I Mech Eng B-J Eng 2015;231:1961–71. https://doi.org/10.1177/0954405415617928.